Transnational University Limburg is a unique collaboration of two universities in two countries: the University of Hasselt and Maastricht University.

UHASSELT
KNOWLEDGE IN ACTION

www.uhasselt.be
Universiteit Hasselt
Campus Hasselt:
Martelarenlaan 42 | 3500 Hasselt
Campus Diepenbeek:
Agoralaan Gebouw D | 3590 Diepenbeek

UHASSELT
KNOWLEDGE IN ACTION

Maastricht University

Faculty of Medicine and Life Sciences
School for Life Sciences
Master of Biomedical Sciences

Master's thesis

Targeting Oxidative Stress in Head and Neck Cancer: From Redox Profiling to ROS-Responsive Drug Delivery

Lise Van Horebeek

Thesis presented in fulfillment of the requirements for the degree of Master of Biomedical Sciences, specialization Molecular Mechanisms in Health and Disease

SUPERVISOR :
Prof. dr. Esther WOLFS

MENTOR :
Mevrouw Nuran CAZ

2024
2025

UHASSELT
KNOWLEDGE IN ACTION

Maastricht University

Faculty of Medicine and Life Sciences
School for Life Sciences
Master of Biomedical Sciences

Master's thesis

Targeting Oxidative Stress in Head and Neck Cancer: From Redox Profiling to ROS-Responsive Drug Delivery

Lise Van Horebeek

Thesis presented in fulfillment of the requirements for the degree of Master of Biomedical Sciences, specialization Molecular Mechanisms in Health and Disease

SUPERVISOR :

Prof. dr. Esther WOLFS

MENTOR :

Mevrouw Nuran CAZ

Targeting Oxidative Stress in Head and Neck Cancer: From Redox Profiling to ROS-Responsive Drug Delivery*

Lise Van Horebeek[1], Nuran Caz[1], Emilie Streel[1] Marnix Persy[2], Anitha Ethirajan[2], and Esther Wolfs[1]

[1]Hasselt University, Biomedical Research Institute (BIOMED), Laboratory for Functional Imaging and Research on Stem Cells (FIERCE Lab), Diepenbeek, Belgium
[2]Nanobiophysics and Soft Matter Interfaces (NSI), Institute for Materials research (IMO-IMOMEC), IMEC, Universiteit Hasselt, Wetenschapspark 1 3590 Diepenbeek

*Running title: *Targeting Oxidative Stress in Head and Neck Cancer*

To whom correspondence should be addressed: Esther Wolfs, Tel: +32 (11) 26 92 96; Email: esther.wolfs@uhasselt.be

Keywords: Redox balance, head and neck cancer, targeted therapy, drug delivery, nanomedicine

ABSTRACT

Head and neck squamous cell carcinoma (HNSCC) is one of the most common types of cancer worldwide. Standard therapies, including chemotherapy, lack selectivity, affecting both cancer cells and healthy tissue, and leading to severe side effects that reduce the patient's quality of life. Nanomedicine offers a promising alternative due to its potential for targeted drug delivery and enhanced drug stability. This study focuses on reactive oxygen species (ROS)-responsive nanocarriers (NCs) that are designed to release their chemotherapeutic cargo in the HNSCC tumor environment, which is characterized by elevated ROS levels. To evaluate the therapeutic potential of these NCs in HNSCC, we first characterized the redox state across a panel of fast-, intermediate-, and slow-growing HNSCC cell lines, including an HPV-positive line. Flow cytometry and confocal microscopy revealed distinct redox profiles, with intermediate-growing cells generally exhibiting a redox balance shifted toward oxidative stress. Fast-growing cells also showed elevated oxidative stress by confocal analysis and in *in vivo* mouse xenograft models, suggesting their potential susceptibility to ROS-responsive therapies. Moreover, the biocompatibility and efficacy of cisplatin-loaded ROS-responsive NCs were assessed. The NCs demonstrated efficient uptake by HNSCC cells and showed a dose-dependent trend toward reduced cell viability, though cell death was limited, indicating a need for further optimization. Nonetheless, with continued development, ROS-responsive NCs hold promise as a more selective and less toxic alternative to conventional chemotherapy in HNSCC.

INTRODUCTION

Head and neck cancer is the seventh most prevalent cancer globally, with an estimated 760,000 new cases in 2022 and a projected increase to 1.5 million cases by 2050 (1-3). These malignancies originate from the oral cavity, pharynx, larynx, paranasal sinuses, nasal cavity, salivary glands, or lips (4, 5). Since most of these sites are lined with mucosal epithelium, around 90% of head and neck cancers originate from this tissue and are thus classified as head and neck squamous cell carcinoma (HNSCC) (3, 6). Major risk factors associated with HNSCC include consumption of alcohol and tobacco and infection with the human papillomavirus (HPV) (7, 8). Once HNSCC is developed, patients may present non-healing sores, painless masses, voice changes, and difficulty or pain when swallowing, among others (2).

Despite improvements in diagnostics, HNSCC is often diagnosed at late stages. This is mainly attributed to the shortcoming of reliable biomarkers, their hidden anatomical sites, frequent misdiagnosis, and disease heterogeneity, which includes variations in tumor genetics, anatomical

location, and clinical presentation (9-11). Consequently, survival rates remain poor, with five- and ten-year overall survival rates of 46% and 31%, respectively (4, 12). Meanwhile, the incidence of HNSCC continues to rise, contributing to increased mortality (3). Prognosis is affected by several factors, including age, race, smoking history, and HPV status, with HPV-positive (HPV+) tumors typically associated with better outcomes (13).

Currently, treating HNSCC often requires a multimodal approach, including surgery, chemotherapy, radiotherapy, and immunotherapy, depending on the stage and the anatomical site of the tumor (4, 12). However, these standard-of-care treatments are associated with severe systemic toxicities, significantly affecting the patient's daily life. Chemotherapy, in particular, lacks selectivity for cancer cells and, hence, also affects fast-dividing healthy cells. This, in turn, results in severe adverse effects such as nausea, alopecia, hepatotoxicity, diarrhea, and mucositis (14).

Although advances in surgical and radiotherapy techniques have improved the therapeutic efficacy and minimized toxicity, significant challenges still exist. Transoral robotic surgery and laser resections are often still associated with dysphagia in 40-80% of patients (15-17). Similarly, innovative radiotherapy techniques, including intensity-modulated radiotherapy, altered fractionation, and stereotactic body radiation therapy, have enhanced precision and reduced toxicity to salivary glands, yet side effects such as acute toxicity persist (16, 18-21). Immune checkpoint inhibitors have also revolutionized cancer therapy. However, response rates remain low in HNSCC, resulting in immune-related side effects (12). These current limitations highlight the urgent need for novel treatment strategies that improve survival, minimize toxicity, and enhance patients' quality of life.

Given these challenges, the tumor microenvironment (TME) has emerged as a potential therapeutic target due to its role in cancer progression. Besides the many cell types in the TME, signaling molecules such as reactive oxygen species (ROS) play a crucial role (22). ROS are highly reactive byproducts of cellular metabolism and consist of numerous molecules such as hydrogen peroxide (H_2O_2), singlet oxygen ($^1O_2$), superoxide (O_2-), and hydroxyl radicals (HO•) (23, 24). Together with the antioxidant system, ROS contributes to the redox balance, which is known to maintain healthy cell signaling. In the TME, ROS can exhibit a dual role. At low or moderate levels, ROS is pivotal in cell signaling and is involved in proliferation and differentiation (24, 25). Higher levels of ROS, however, can disrupt the redox balance, leading to oxidative stress. This results in macromolecular damage to DNA, proteins, and lipids, ultimately leading to cell senescence or oxidative cell death (23, 24).

This dysregulated redox state creates a promising opportunity for cancer therapies (23, 24, 26, 27). In particular, HNSCC is characterized by elevated levels of ROS, along with alterations in the antioxidant defense system (28-30), indicating a disrupted redox balance (28, 29, 31). Conventional treatment approaches, such as chemotherapy, already rely on cell death induced by oxidative stress, but have poor tumor selectivity (24, 32). Developing therapies that further increase ROS levels or disrupt the tumor's antioxidant defenses can tip the redox balance toward oxidative cell death, selectively targeting cancer cells while sparing healthy tissue (24, 26).

One such strategy is the ROS-dependent, FDA-approved photodynamic therapy (PDT), which utilizes a photosensitizer that converts oxygen into ROS upon exposure to light. While PDT effectively increases oxidative stress in cancer cells, its use is restricted by poor tissue penetration, limiting treatment of deeper tumors, and potential collateral damage to surrounding healthy tissue, such as burns, edema, and ulcers (26, 33).

More recently, non-thermal plasma (NTP) has emerged as a highly investigated ROS-based therapy. NTP generates an ionized gas rich in ROS. By exploiting the inherently high ROS levels in HNSCC cells, NTP selectively induces oxidative stress in the tumors with minimal impact on healthy tissue (34). However, challenges remain, including potential genotoxicity, collateral edema, and hemorrhage (35, 36).

Nanomedicine is a widely investigated field in cancer research, utilizing nanotechnology for the diagnosis, treatment and prevention of diseases

(37). Nanomedicine offers several advantages in oncology, such as targeted drug delivery and enhanced drug stability (38). Nanocarriers (NCs) can be designed to release their cargo in response to exogenous or endogenous stimuli. Exogenous stimuli include light or radiation, while endogenous stimuli exploit features of the TME such as pH levels, hypoxia, or disrupted redox balance (39, 40). Therefore, ROS-responsive NCs provide a particularly promising approach, leveraging the high ROS levels in HNSCC to selectively release anticancer drugs (28). This targeted drug delivery system aims to minimize systemic toxicity while enhancing treatment efficacy (23). Although preclinical studies have demonstrated promising results in breast cancer and prostate cancer, several challenges remain for clinical translation (41-43). These include ensuring reproducibility during nanoparticle synthesis to minimize batch-to-batch variability, as well as achieving sufficient stability in complex *in vivo* environments to prevent premature drug release and loss of therapeutic efficacy (44).

While these emerging ROS-based therapies hold great promise, critical gaps in our understanding of how redox balance is regulated in HNSCC remain. Tumor heterogeneity suggests that different HNSCC subtypes may exhibit distinct ROS levels and antioxidant capacities, potentially influencing their response to ROS-modulating therapies. Factors such as HPV status, metabolic reprogramming, and variations in oxidative enzyme expression could contribute to these differences (45). A deeper characterization of ROS dynamics is hence crucial for optimizing these ROS-modulating treatments. Moreover, current knowledge of the ROS levels across different HNSCC cell lines remains limited. Therefore, this study aims to investigate the redox status of different HNSCC cell lines *in vitro* and *in vivo*. By mapping baseline ROS levels and antioxidant capacities across various HNSCC subtypes, this research could provide insights crucial to optimizing ROS-exploiting therapies. Furthermore, this study is focused on the assessment of chemotherapy-loaded, ROS-responsive NCs in the treatment of HNSCC. Ultimately, these findings may aid in the development of more targeted and effective treatment strategies, reducing systemic toxicity and improving HNSCC patients' quality of life.

EXPERIMENTAL PROCEDURES

Cell culture – The human HNSCC cell line UM-SCC-14C (CVCL_7721, CLS cell lines service, Germany) was cultured in Dulbecco's Modified Eagle Medium/ Nutrient Mixture F-12 Ham (DMEM/F-12; Thermo Fisher Scientific, USA) supplemented with 5% heat-inactivated Fetal Bovine Serum (FBS; Biowest Avantor, France) and 1% Penicillin/Streptomycin (Pen/Strep; 100 µg/mL streptomycin, 100 U/mL penicillin, Merck, Germany). The HNSCC cell lines Cal-27 (305029, Cytion, Germany), FaDu (HTB-43, ATCC, Germany), SCC-25 (300607, Cytion), UM-SCC-104 (SCC072, Merck), and SCC-9 (CRL-1629, ATCC) were maintained in DMEM high-glucose (Thermo Fisher Scientific) supplemented with 10% heat-inactivated FBS and 1% Pen/Strep. UM-SCC-14C cells were trypsinized using Accutase® solution (Merck) and all other cell lines using trypsin-EDTA (Thermo Fischer Scientific). All cell lines were incubated at 37°C in a humidified atmosphere containing 5% CO2. Cells were counted using the trypan blue dye 0.4% (GibcoTM, Thermo Fisher Scientific, Belgium) exclusion test. All cell lines were tested for mycoplasma contamination and excluded if positive.

Lentiviral transduction of HNSCC cells – Cal-27, UM-SCC-14c, and FaDu cells were transduced using a second-generation lentiviral vector carrying the firefly luciferase (*Fluc*) gene. First, plasmids were amplified in *E. Coli* Stbl3 using the NucleoBond Xtra Midi Plus EF kit (MACHEREY-NAGEL, Germany). Lentiviral particles were produced via transfection of HEK293T cells with the Fluc-plasmid as previously described (46). For transduction, HNSCC cells were seeded at a density of $2{,}5x10^3$ cells/cm² and allowed to adhere overnight. Cells were exposed to 10µL of lentiviral particles for 7 hours. Upon reaching 90% confluency, transduced cells were selected using different puromycin (InvivoGen, France) concentrations for four days: 0.5 µg/mL to Cal-27 and SCC-25 cells, 1 µg/mL to FaDu and UM-SCC-104 cells and 1.5 µg/mL to UM-SCC-14C cells.

In vitro redox analysis

Baseline ROS and antioxidant levels in all cell lines were determined via flow cytometry and confocal microscopy, using redox-sensitive probes (Table 1).

Table 1: redox-sensitive probes

Probe	Concentration (µM)	Ex/em (nm)	Company / reference
2', 7'-Dichlorofluorescin diacetate (DCFDA)	10 µM	485/535	Abcam (UK)
MitoSOX Red	5 µM	396/610	Thermo Fischer
NBD-P	25 µM	470/585	(47)
BODIPY (Image-iT™ Lipid Peroxidation Kit)	10 µM	570/630 & 483/530	Thermo Fischer
ThiolTracker™ Violet	10 µM	404/526	Thermo Fischer

Flow cytometry – Cells were seeded at a density of 23x10³ cells/cm² and allowed to adhere overnight. Cells were trypsinized and centrifuged (5 min, 2000 rpm, 21°C), followed by staining with redox-sensitive probes for 30 min at 37°C (Table 1), and with ZombieNIR viability dye (1:1000; NC0520979, BioLegend, USA) for 20 min at 4°C. Samples were washed three times with phosphate-buffered saline (PBS; VWR) containing 2% FBS with centrifugation steps in between (5 min, 2000 rpm, 4°C). All samples were measured using an LSR Fortessa flow cytometer (BD Biosciences, USA), acquiring 10,000 events per sample. Data were analyzed using the FlowJo software.

Confocal microscopy - Cells were seeded at a density of 15x10³ cells/cm². After overnight attachment, cells were stained with redox-sensitive probes (Table 1) for 30 min at 37°C. Nuclei were counterstained using 0.5% v/v Hoechst 33342 (#639, Antibodies inc, USA) for 10 min at 37°C. The cells were imaged using the LSM 880 confocal microscope (Zeiss, Germany) while maintained at 37°C and 5% CO_2 and analyzed using ImageJ.

In vivo redox analysis

Animals – All animal experiments were performed according to the European Directive 2010/63/EU and approved by the Ethical Committee for Animal experimentation of Hasselt University. Hsd:Athymic Nude-Foxn1^{nu} mice (Envigo, USA) of 6-weeks of age were used to create HNSCC xenograft mouse models by subcutaneously injecting 100 µl of cell suspension into the left flank. The suspension consisted of 50 µL of 1 × 10⁶ transduced cells (UM-SCC-14C, FaDu, or Cal-27) suspended in their respective culture medium and 50 µL of growth factor-reduced Matrigel (Corning, USA). Each experimental group consisted of 4 mice. Mice were euthanized at the end of the study by cervical dislocation.

In vivo imaging - Three days post-tumor inoculation, H_2O_2 and reduced glutathione (GSH) levels in the tumors were assessed every two days using a bioluminescent Peroxy Caged Luciferin-1 (PCL-1) probe and a fluorescent NBD-P probe, respectively. Both probes were synthesized in collaboration with the team of Prof. Wouter Maes, as previously described (47, 48). For each measurement, mice were anesthetized with isoflurane (2% in 100% oxygen at a flow rate of 2 L/min). For H_2O_2 imaging, 50 µL of PCL1 (0.1 mM in 1:1 DMSO:PBS) was injected subcutaneously in close proximity to the tumor, followed by image acquisition every two minutes for one hour at 37°C. For reduced GSH imaging, 100 µL of NBD-P (10 mM in PBS) was injected intratumorally and imaged immediately. Images were acquired using the IVIS Illumina III *In vivo* Imaging System (Revvity, PerkinElmer, USA), and ROIs were defined. Using the Living Image software (Perkin Elmer), the total counts of the ROIs were measured. Tumor volume was determined using a caliper, and body weight was recorded prior to each measurement.

Nanocarrier assessment

NC characterization – The NCs used in this study were synthesized and characterized by the group of Prof. Anitha Ethirajan (IMO-IMOMEC UHasselt) as previously described (48). Briefly, the NCs contain a dextran polysaccharide shell linked with thioketal moieties, enabling ROS responsiveness. The NC payloads consisted of either Rhodamine B (RhoB) or a complex of cisplatin-hyaluronic acid (Cis-HA). The hydrodynamic diameter of the NCs was determined using dynamic light scattering and measured 156 nm and 160 nm for the RhoB-NCs and the Cis-HA NCs, respectively. The RhoB-NCs and the Cis-HA NCs showed a polydispersity index of 0.12 and 0.13 and a solid content of 5200 and 6800 µg/mL, respectively. The Cis-HA-NCs had an encapsulation efficiency of 88% and a drug loading

content of 91 µg/mL. The Cis-HA complex was synthesized by mixing cisplatin (C2210000, Merck) with sodium hyaluronate in a 1:1 molar ratio in MilliQ water. The mixture was stirred at 400 rpm for 4 hours at 37°C.

Cell viability – UM-SCC-14C cells were seeded at a density of $15x10^3$ cells/cm², allowed to adhere overnight, and treated with various concentrations of the Cis-HA complex (1-100 µg/mL), or Cis-HA or Rhodamine B (RhoB) - loaded NC (0–750 µg/mL). The alamarBlue (BUF012B, Bio-Rad, USA) cell viability assay was performed after 24 h, 48 h and 72 h of incubation, according to the manufacturer's instructions. Fluorescent intensity was measured at Ex/Em 540/590 nm wavelength using the CLARIOstar plus plate reader (BMG Labtech, Germany). Data were normalized to the negative control and represented as relative percentages of cell viability.

NC uptake - NC uptake was assessed using confocal microscopy. UM-SCC-14C cells were seeded at a density of $15x10^3$ cells/cm² on glass coverslips, attached overnight, and treated with 100 or 200 µg/mL RhoB-loaded NCs for 24, 48, or 72 h (UM-SCC-14C). Cells were fixed using 4% paraformaldehyde for 20 min. Next, the cell membrane was stained with wheat germ agglutinin AlexaFluor 647 (11510826, WGA647, 1/200, InvitrogenTM, Thermo Fisher Scientific, Belgium) and the nuclei with 4',6-diamidino-2-phenylindole (DAPI, 1/10000, Thermo Fisher Scientific) in PBS for 10 min. Coverslips were mounted on microscopic slides using Fluoromount-G™ mounting medium (Thermo Fisher Scientific). Representative images were obtained using the LSM900 confocal microscope (Zeiss, Germany), and images were processed using the ZEN Blue software.

Statistical analysis – Normality and equal variances were assessed using the Shapiro-Wilk and Brown-Forsythe tests, respectively. Normally distributed data were analysed using one-way ANOVA (*in vitro* redox) or two-way ANOVA (*in vivo* and NC studies), followed by Tukey's post hoc test. Non-normally distributed data were analysed with the Kruskal-Wallis test. Statistical analysis was performed using GraphPad Prism version 10.5.0. Data are represented as mean ± SEM, with p-values ≤ 0.05 considered statistically significant.

RESULTS

In vitro redox characterization of HNSCC revealed differences in redox balance across cell lines – The redox balance was assessed by measuring general ROS levels and mitochondrial superoxide as a marker of oxidative stress and reduced GSH levels as an indicator of the antioxidant capacity. The levels of these markers, together with lipid peroxidation to evaluate oxidative damage, were quantified by flow cytometry (Fig. 1). These analyses showed that the fast-growing cell lines Cal-27 and FaDu (Fig. 1A, B) exhibited a more balanced redox state, whereas intermediate-growing UM-SCC-14C (Fig. 1C) and slow-growing SCC-25 and SCC-9 cells (Fig. 1D, E) showed a shift toward oxidative stress. The HPV+ UM-SCC-104 cells displayed a redox profile tipped toward antioxidant defense (Fig. 1F).

When comparing among the different cell lines, intermediate growing cells showed a trend toward elevated general ROS levels, as measured by DCFDA, compared to fast-growing and HPV+ cells (Fig. 1G). Slow-dividing cells exhibited varying general ROS levels, with SCC-25 cells having high and SCC-9 cells moderate levels compared to the other cell lines. Conversely, HPV+ UM-SCC-104 cells showed higher levels of reduced GSH, an important antioxidant measured using NBD-P, compared to HPV- lines, although the difference was not statistically significant. Additionally, lipid peroxidation was measured as an indicator of oxidative damage (Fig. 1H). This was elevated in HPV+ cells compared to HPV- cells. Fast-growing cells exhibited the lowest ratio of oxidized to reduced lipids, suggesting the least oxidative damage.

The redox balance was further investigated using confocal microscopy to visualize the redox-sensitive probes. Fast-growing Cal-27 and FaDu cells, as well as intermediate-growing UM-SCC-14C cells exhibited high levels of general ROS and low levels of reduced GSH, indicating elevated oxidative stress (Fig. 2 A-C). Slow-growing SCC-25 and SCC-9 cells displayed a more balanced redox state with a slight shift toward oxidative stress

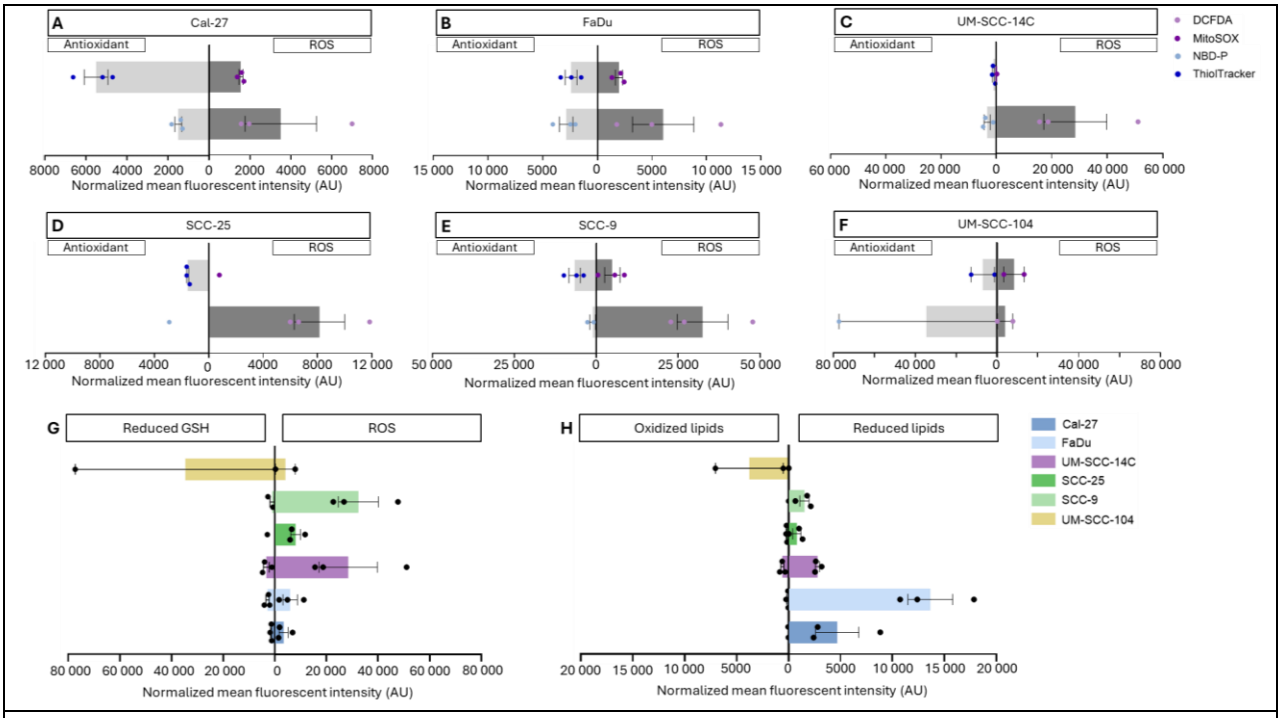

Fig. 1 –The basal redox balance was profiled across different HNSCC cell lines. Redox-sensitive fluorescent probes were used to assess antioxidant capacity and ROS levels in various HNSCC cell lines by flow cytometry. (**A-F**) The mean fluorescent intensity of each probe was quantified. For each cell type, the antioxidant capacity is plotted on the left side, whereas the ROS levels are plotted on the right side. (**G**) The redox balance is shown for all HNSCC cell lines with general ROS levels measured by DCFDA and glutathione levels measured by NBD-P. (**H**) Lipid peroxidation is shown as the balance of oxidized lipids (FITC) and reduced lipids (7-AAD), measured by Bodipy. **(A-H)** Data are normalized to unstained controls and represented as mean ± SEM. n=3 biological replicates; UM-SCC-104: n=2 biological replicates. **(G,H)** Data were analyzed using One-way ANOVA. *DCFDA:* 2', 7'-Dichlorofluorescin diacetate*, GSH: glutathione , ROS: reactive oxygen species.*

due to increased mitochondrial superoxide levels, as measured by MitoSOX Red (Fig. 2D,E). The HPV+ UM-SCC-104 cells also showed clear signs of oxidative stress, with elevated general ROS and mitochondrial superoxide levels, and low levels of the antioxidant reduced GSH (Fig. 2F), as observed in the representative images (Fig. 2G).

When comparing the redox state across all cell lines, fast-growing Cal-27 and FaDu, intermediate-growing UM-SCC-14C, and HPV+ UM-SCC-104 cells all exhibited a disturbed redox balance, characterized by high levels of general ROS, measured by DCFDA, and low levels of reduced GSH (Fig. 2H). Slow-growing SCC-25 and SCC-9 cells had higher levels of reduced GSH. Due to the relatively high ROS levels in SCC-25 and low ROS levels in SCC-9, these lines respectively maintained a balanced redox state or a redox state tipped towards increased antioxidant levels.

Lastly, lipid peroxidation was assessed via confocal microscopy. Quantification revealed that SCC-25 and Cal-27 cells maintained a relatively balanced lipid peroxidation ratio, with comparable levels of oxidized and reduced lipids (Fig. 3A). Slow-growing SCC-25 cells showed high levels of both oxidized and reduced lipids, while fast-growing Cal-27 cells had low levels of both, resulting in relatively low levels of lipid peroxidation in both lines. In contrast, Slow-growing SCC-9, intermediate-growing UM-SCC-14C, and fast-growing FaDu cells all exhibited slightly higher levels of oxidized lipids compared to reduced lipids, indicating a modest shift toward lipid peroxidation and suggesting low levels of oxidative damage. However, HPV+ UM-SCC-104 cells displayed the most pronounced imbalance, with substantially lower levels of reduced lipids and moderately elevated oxidized lipids, resulting in a

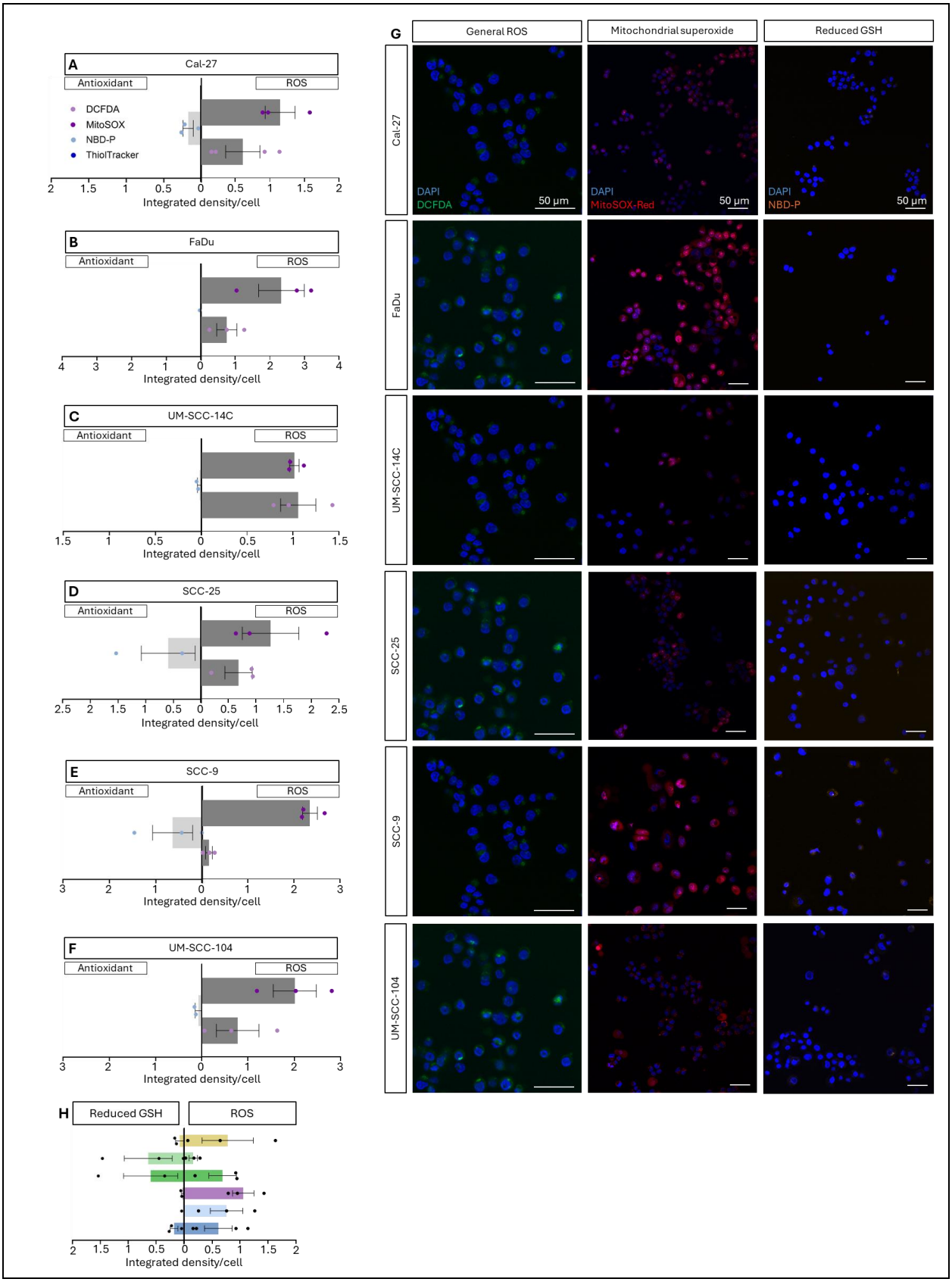
A
Cal-27
Antioxidant
ROS
DCFDA
MitoSOX
NBD-P
ThiolTracker
Integrated density/cell
B
FaDu
C
UM-SCC-14C
D
SCC-25
E
SCC-9
F
UM-SCC-104
H
Reduced GSH
ROS
G
General ROS
Mitochondrial superoxide
Reduced GSH
DAPI
DCFDA
MitoSOX-Red
NBD-P
50 µm

Fig. 2 – Redox profiles across different HNSCC cell lines. Redox-sensitive fluorescent probes were used to visualize antioxidant levels and ROS levels in various HNSCC cell lines by confocal microscopy. (**A-F**) The integrated density per cell of each probe was quantified and normalized to unstained images. For each cell type, the antioxidant capacity is plotted on the left side, whereas the ROS levels are plotted on the right side. (**G**) Representative images of DCFDA, MitoSOX-Red, and NBD-P for each cell line. (**H**) The redox balance is shown for all HNSCC cell lines with general ROS levels measured by DCFDA and glutathione levels measured by NBD-P. (**A-F, H**) Data are normalized to unstained controls and represented as mean ± SEM. n=3 biological replicates. (**H**) Data were analyzed using a Kruskal-Wallis test: DCFDA, and a one-way ANOVA; NBD-P. *DCFDA:* 2', 7'-Dichlorofluorescin diacetate*, GSH: glutathione, ROS: reactive oxygen species.*

higher oxidized-to-reduced lipid ratio and increased lipid peroxidation, as observed in the representative images (Fig. 3B,C).

In vivo redox characterization of HNSCC showed varying levels of ROS and reduced GSH across cell lines – To gain more insights into the heterogeneity of the redox balance in HNSCC, an *in*

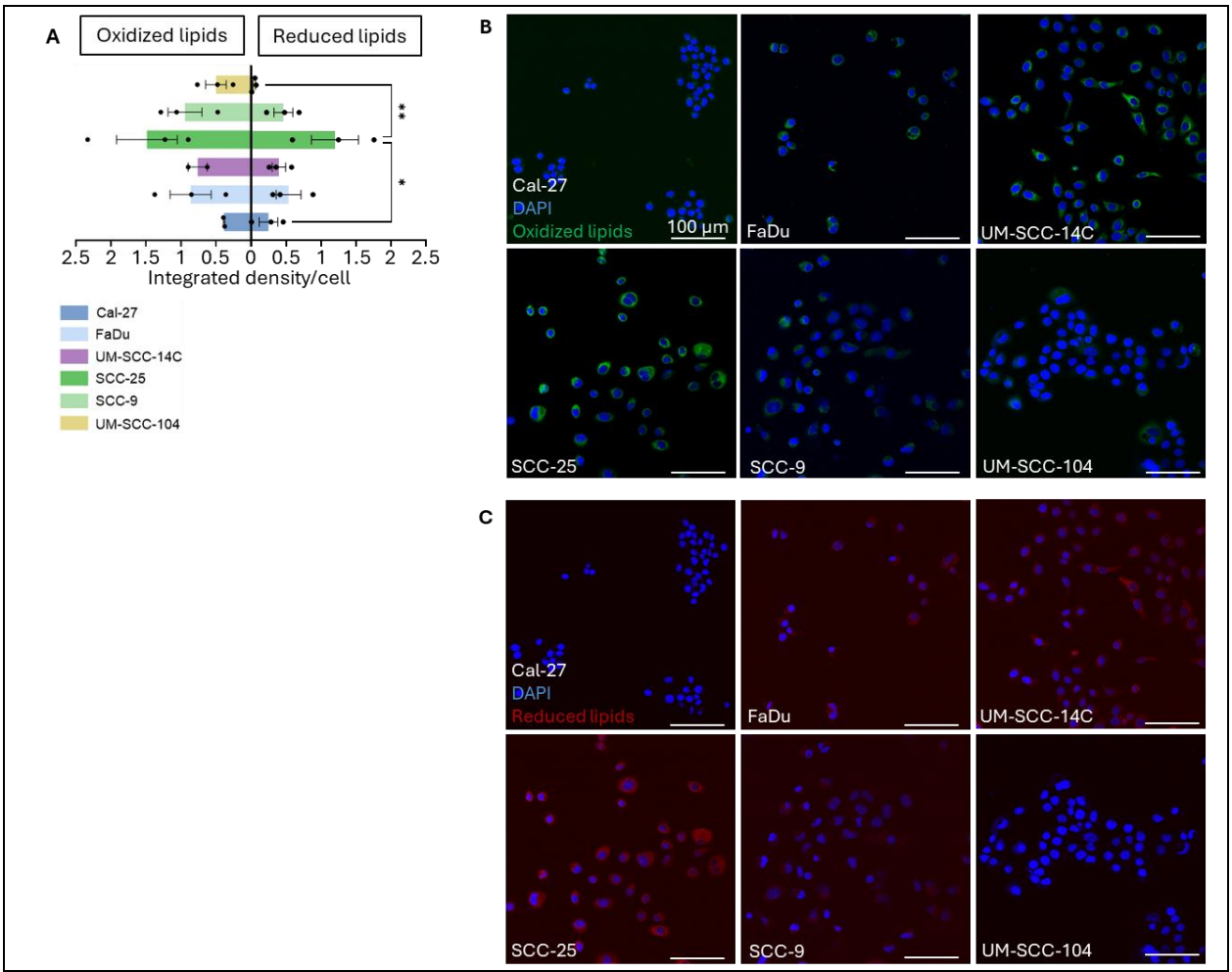

Fig. 3 – Lipid peroxidation levels vary across different HNSCC cell lines. (**A**) Balance of oxidized lipids (FITC) and reduced lipids (7-AAD), quantifying lipid peroxidation in different HNSCC cell lines, measured by Bodipy. Representative images of (**B**) oxidized lipids, and (**C**) reduced lipids, visualized using confocal microscopy. Data are normalized to unstained controls and represented as mean ± SEM. n=3 biological replicates; n=2 biological replicates UM-SCC-14C and Cal-27 oxidized lipids. (**C**) Data were analyzed using a one-way ANOVA. * $p < 0.05$, ** $p < 0.1$.

vivo study was performed to unravel these differences in a more physiologically complex environment. For this, an HNSCC xenograft mouse model was generated in which mice were inoculated with transduced Fluc+ Cal-27, FaDu, or UM-SCC-14C cells. Expression of firefly luciferase in these cells was essential since the PCL-1 probe, which detects H_2O_2, depends on this enzyme to perform its function. The three cell lines were selected since these are the utmost aggressive HNSCC cell lines.

Figure 4A shows the study timeline for the *in vivo* redox characterization in the three different HNSCC xenograft models. H_2O_2 levels were measured over time and were found to increase in all xenografts (Fig. 4B). FaDu tumors displayed significantly higher H_2O_2 levels at later time points

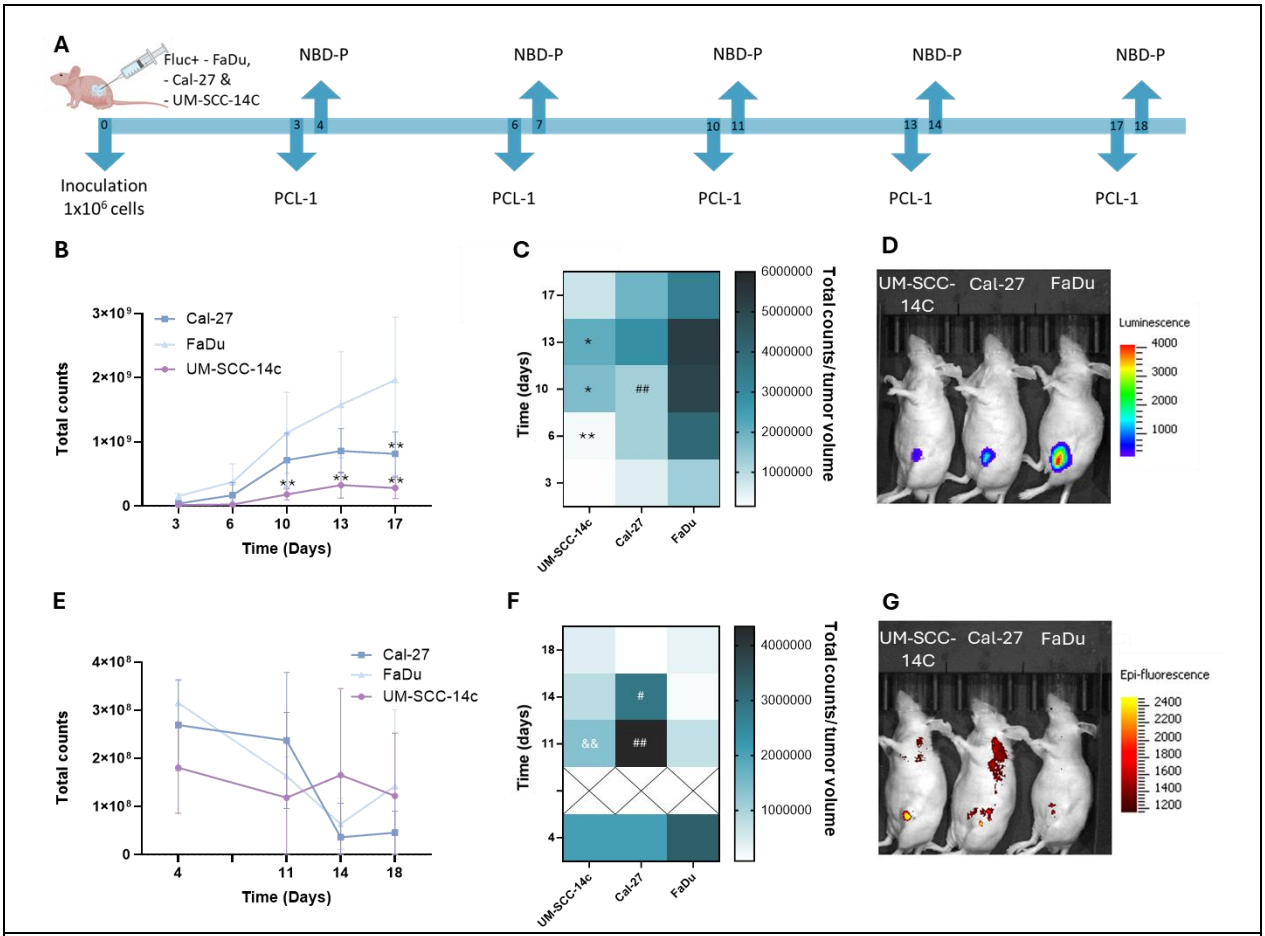

Fig. 4 – H_2O_2 and reduced GSH levels vary across different HNSCC mouse xenografts. (**A**) Experimental timeline showing inoculation with Fluc⁺ HNSCC cells and *in vivo* imaging timepoints. (**B**) Peak bioluminescent signal in mice subcutaneously injected with PCL-1 (0.1 mM in 50 µL of 1:1 DMSO:PBS), integrated over 1 hour. PCL-1 signal reflects H_2O_2 levels and was measured using the IVIS Lumina III. (**C**) Ratios of total PCL-1 signal to tumor volume at the corresponding timepoint. (**D**) Representative IVIS images of one mouse per group post-PCL-1 injection. (**E**) Total counts of fluorescence in mice injected with NBD-P (10 mM in 100 µL of PBS, intratumoral injection), measured immediately after injection. (**F**) NBD-P fluorescence intensity normalized to tumor volume at the corresponding timepoint. **(G)** Representative fluorescent images of mice post-NBD-P injection. Data presented as mean ± SEM. n=3-4 biological replicates. Data analyzed using two-way ANOVA, followed by Tukey's post-hoc test. *: $p < 0.05$ and **: $p < 0.001$. *: statistical difference between UM-SCC-14C and FaDu cells, #: statistical difference between Cal-27 and FaDu cells, and &: statistical difference between UM-SCC-14C and Cal-27 cells. *Fluc: firefly luciferase, GSH: glutathione, PCL-1: peroxy-caged luciferin.*

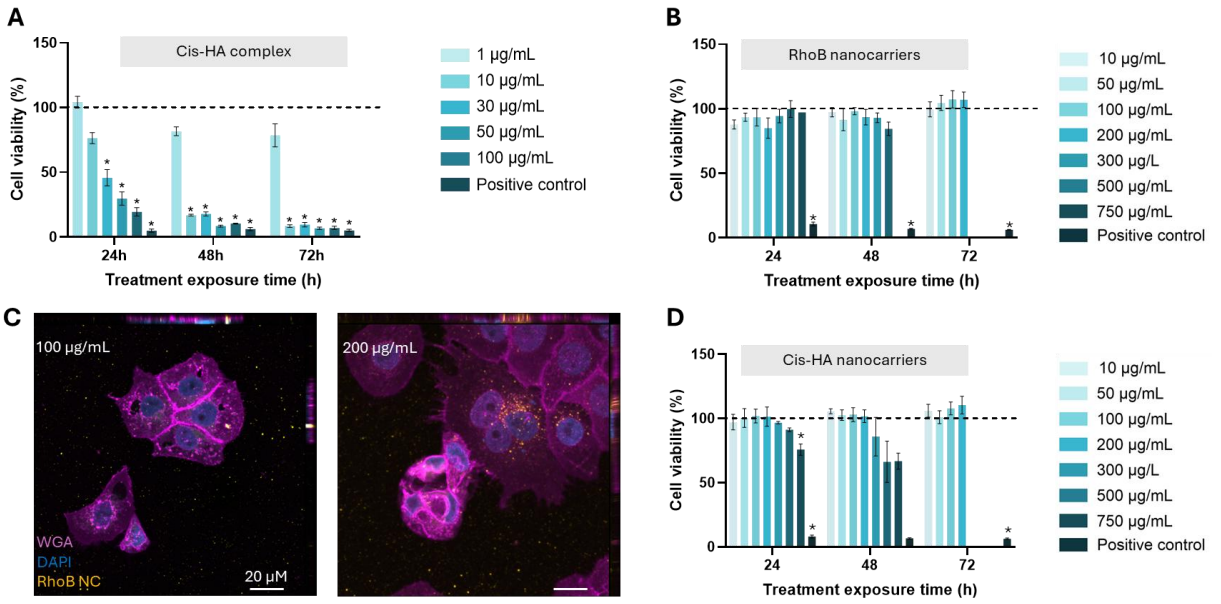

Fig. 4 – Cis-HA complex induces cytotoxicity, whereas minimal cytotoxicity was observed in cis-HA-loaded NCs. Cell viability of UM-SCC-14C cells treated with different concentrations of (**A**) the cis-HA complex, and (**B**) the Rhodamine B-loaded NCs, measured using an alamarBlue assay. The dotted line represents a negative untreated control. (**C**) Uptake of Rhodamine B loaded NCs into UM-SCC-14C cells after 24 hours of treatment. The cells were counterstained with DAPI to visualize the nuclei and with WGA to visualize the cell membrane. (**D**) Cell viability of UM-SCC-14C cells treated with different concentrations of Rhodamine B-loaded NCs. The dotted line represents a negative untreated control. Data are represented as mean ± SEM. n=3 biological replicates; n=1 RhoB NCs 750 µg/mL. Data were analyzed using a one-way ANOVA or Kruskal-Wallis test. * $p < 0.05$. *Cis-HA: cisplatin – hyaluronic acid, NC: nanocarrier, RhoB: Rhodamine B, WGA:Wheat Germ Agglutinin.*

compared to UM-SCC-14C and Cal-27 tumors, reflecting high ROS levels.

To account for differences in tumor size, the bioluminescent signal was normalized to tumor volume (Fig. 4C). The normalized data showed a similar trend to the non-normalized values, with FaDu tumors exhibiting significantly higher H_2O_2 levels compared to Cal-27 and UM-SCC-14C tumors. However, in contrast to the non-normalized data, the final time point showed a decrease in H_2O_2 levels across all xenograft models. Representative images of the bioluminescent signal also indicate increased H_2O_2 levels in the FaDu xenograft model (Fig. 4D).

Reduced GSH levels showed a decreasing trend during tumor expansion in Cal-27 and FaDu xenografts, while being more stable in UM-SCC-14C xenografts (Fig. 4E). When normalized to tumor volume, Cal-27 tumors showed significantly higher levels of reduced GSH compared to UM-SCC-14C tumors at day 11 post-inoculation and to FaDu tumors at day 11 to 14 post-inoculation (Fig. 4F). Representative images of the fluorescent signal of the NBD-P probe are shown in Figure 4G.

ROS-responsive NCs are efficiently internalized by HNSCC cells, and cytotoxic when loaded with chemotherapeutic cargo – Cisplatin is a widely used chemotherapeutic agent for HNSCC but suffers from poor aqueous solubility, limiting the amount that can be effectively encapsulated within NCs. To address this limitation, cisplatin was conjugated to HA to form a more soluble Cis-HA complex. The cytotoxic potential of this complex was first evaluated to ensure that cisplatin retained its antitumor activity after conjugation. In UM-SCC-14C cells, 24-hour treatment with Cis-HA at concentrations of 30, 50, and 100 µg/mL led to significant reductions in cell viability compared to untreated controls (Fig. 5A). At 48 and 72 hours, even 10 µg/mL of Cis-HA significantly decreased viability, indicating that the conjugate retained the cytotoxic efficacy of cisplatin and could serve as a viable therapeutic payload in ROS-responsive NCs.

Next, it was crucial to determine the biocompatibility and uptake rate of the designed NCs. Treatment with RhoB-loaded NCs did not significantly affect UM-SCC-14C cell viability (Fig. 5B). A slight reduction in viability was observed at the highest tested concentration (500 µg/mL), but this was not statistically significant, confirming the NCs themselves are non-toxic and biocompatible. Fluorescence imaging revealed substantial uptake of RhoB-NCs after 24 hours, particularly at the 200 µg/mL concentration condition (Fig. 5C). These findings demonstrate that the NCs are efficiently internalized by HNSCC cells and are capable of reaching intracellular ROS-rich environments where release of chemotherapeutic cargo should occur.

Finally, the therapeutic potential of Cis-HA-loaded NCs was assessed. Despite clear cellular uptake, a significant reduction in UM-SCC-14C cell viability was observed only after 24 hours of treatment with the highest concentration tested (750 µg/mL) (Fig. 5D). Although not significant, treatment with 500 and 750 µg/mL of the Cis-HA-loaded NCs also resulted in decreased cell viability at 48 hours, indicating the cytotoxic potential of these ROS-responsive NCs. These results suggest that while the NCs are effectively internalized and the Cis-HA payload retains its cytotoxic potential in free form, the encapsulated form may require optimization to improve its therapeutic potential.

DISCUSSION

Chemotherapy remains a standard treatment for HNSCC, but its lack of selectivity, leading to systemic toxicity and severe side effects (14). As a result, nanomedicine has emerged as a promising strategy to improve therapeutic precision while minimizing off-target damage. In particular, stimuli-responsive NCs offer the advantage of releasing chemotherapeutic agents specifically in the TME, where unique biochemical stimuli such as elevated ROS levels can be exploited (28-30, 38-40). This study focused on ROS-responsive NCs, designed to trigger drug release in response to high ROS levels typically found in HNSCC tumors. To optimize the ROS-responsive NCs and to identify which tumor subtypes might be most susceptible to this treatment approach, we first characterized the redox state of several HNSCC cell lines representing aggressive, intermediate, slow-growing, and HPV-positive subtypes, and evaluated the uptake and therapeutic potential of ROS-responsive NCs.

The *in vitro* redox characterization revealed varying results when comparing data obtained by flow cytometry and confocal microscopy, which may stem from the dynamic and adaptive nature of the redox regulation within cells (49). For instance, UM-SCC-104 cells exhibited high ROS levels in confocal microscopy but lower ROS levels and higher antioxidant activity by flow cytometry. This suggests that these cells respond to oxidative stress by activating antioxidant defenses, potentially via redox-sensitive pathways such as Keap1-Nrf2 (50). Elevated lipid peroxidation in UM-SCC-104 cells further supports the presence of ongoing oxidative stress. Similarly, the rapidly proliferating Cal-27 and FaDu cell lines exhibited low ROS levels and lipid peroxidation by flow cytometry, but confocal analysis revealed elevated ROS and reduced GSH levels, and signs of oxidative damage. This suggests that chronic oxidative stress may have led to antioxidant depletion and secondary ROS accumulation.

Additionally, technical differences may also contribute to these differences between techniques. Flow cytometry measures cells in suspension following trypsinization, whereas confocal microscopy assesses live adherent cells. It has previously been indicated that detachment through trypsinization can transiently increase intracellular ROS levels, and that cellular redox states can shift during transition from adherent to suspended states (51, 52). Furthermore, the mechanical stress induced during sample preparation for flow cytometry can trigger stress-related biochemical changes, while cells imaged via confocal microscopy were maintained under stable conditions (37°C and 5% CO_2), providing more physiological conditions (53).

Not only was variability between experiments observed, but within experiments, biological replicates also showed notable variations. Part of this variation may be attributed to differences in cell cycle distribution. ROS levels are known to fluctuate throughout the cell cycle, with higher levels typically observed during the G2 and M phases and lower levels during G1 (54). As cells in this study were not synchronized, and the cell cycle

phase was not assessed during redox characterization, this may have introduced variability into the measurements. While these findings provide meaningful insight into redox imbalances across different HNSCC subtypes, future studies should control for cell cycle phase in order to allow for a more accurate assessment of intrinsic redox differences, independent of proliferation phase.

The *in vivo* study revealed high ROS levels in fast-growing tumor xenografts, which increased over time. However, following normalization to tumor volume, a slight decrease in H_2O_2 levels was observed at the final time point across all tumors, a trend not seen in the non-normalized values. This suggests that the observed increase in raw signal over time may, in part, reflect tumor growth rather than a continued rise in ROS production. Despite this decrease, the elevated ROS levels in fast-growing cells suggest their potential susceptibility to ROS-targeted therapies. UM-SCC-14C cells consistently displayed a pro-oxidative redox state across both flow cytometry and confocal microscopy, marked by high ROS levels and low intracellular GSH. This would suggest sensitivity to ROS-responsive therapies. However, *in vivo* data showed lower ROS signals in UM-SCC-14C tumors compared to fast-growing lines like Cal-27 and FaDu.

These discrepancies between *in vitro* and *in vivo* data may be attributed to key features of the TME, such as hypoxia, which are known to significantly influence redox dynamics *in vivo* but are absent in *in vitro* cultures (55). Additionally, the *in vivo* and *in vitro* studies assessed different parameters. ROS levels *in vitro* were evaluated by DCFDA and Mitosox-Red, respectively measuring general ROS and mitochondrial superoxide levels, while ROS levels *in vivo* were evaluated using the PCL-1 probe, measuring H_2O_2. Therefore, future studies applying the PCL-1 probe *in vitro* could provide more comparable results.

Reduced GSH measurements provided further insight into redox heterogeneity by assessing the antioxidant capacity. The *in vivo* study revealed higher levels of reduced GSH in Cal-27 tumors compared to UM-SCC-14C and FaDu tumors, which is in line with the data obtained by confocal microscopy. However, flow cytometry analysis indicated the lowest levels of reduced GSH in Cal-27 cells, once again highlighting the variability between the techniques.

Beyond redox characterization, this research also focused on the implementation of ROS-responsive NCs. The biocompatibility and uptake of RhoB-loaded NCs and the efficacy of Cis-HA-loaded NCs to induce cell death were simultaneously assessed. Cisplatin is known to have poor solubility and stability in aqueous solutions (56). Therefore, it was conjugated with HA, which has high water-retaining abilities, to increase its loading concentration (57). Due to its natural occurrence in the body, HA is highly biocompatible and FDA-approved, making it suitable for biomedical use (58). The anticancer activity of the Cis-HA complex was confirmed in cell viability assays using UM-SCC-14C cells, which were selected for their intermediate growth rate. This aligns with previous studies where Cis-HA complexes were also exhibited therapeutic efficacy in breast cancer cell lines (59). Therefore, the Cis-HA conjugate is compatible with serving as the cargo of the ROS-responsive NCs.

The ROS-responsive NCs used in this research consist of dextran shells with thioketal moieties. Dextran is a natural polysaccharide, offering several advantages, including biocompatibility and easy surface and size modification (60). The thioketal linkages are ROS-responsive and will be cleaved upon exposure to ROS, resulting in a thiol-containing and acetone group (61). Incorporating thioketal linkages enhances the specificity of NCs to the tumor environment while maintaining biodegradability and biocompatibility.

The RhoB-loaded NCs demonstrated efficient cellular uptake in UM-SCC-14C cells, particularly at higher concentrations. This is consistent with other reports of successful ROS-responsive polymer-based NCs uptake in HNSCC cells (62). The therapeutic efficacy of ROS-responsive Cis-HA-loaded NCs was evaluated in UM-SCC-14C cells. While treatment resulted in a dose-dependent decrease in cell viability, a statistically significant reduction was observed only at the highest concentration (750 µg/mL) at a single time point. Nonetheless, the observed trend toward reduced cell viability when treated with 500 or 750 µg/mL highlights the cytotoxic potential of this drug

delivery system. Previous studies have reported ROS-responsive chemotherapy-loaded NCs and pro-oxidant cancer therapy-loaded nanoparticles to have resulted in successful *in vitro* cell death of HNSCC and breast cancer cells, respectively (62, 63). Moreover, Nayak S. et al. revealed the cytotoxic potential of dextran-based ROS-responsive doxorubicin-loaded NCs (48). The current findings support this line of research and indicate that ROS-triggered release mechanisms remain a viable strategy, while also underscoring the need for further optimization to enhance drug release and therapeutic efficacy.

To enable clinical translation of ROS-responsive NCs, future studies should include the evaluation of *in vivo* biodistribution, tumor accumulation, and efficacy. Evaluating how the NCs distribute in tumor tissue compared to healthy tissue and determining their therapeutic efficacy in animal models will be crucial steps in validating their safety and effectiveness. Additionally, incorporating other characteristics of the TME, such as pH or intracellular GSH concentrations, could potentially improve tumor targeting. Next to this, NC responsiveness could be fine-tuned or even personalized to match the redox status of specific tumor subtypes, potentially increasing therapeutic impact while minimizing off-target effects. Lastly, the current ROS-responsive NC formulation could be evaluated in additional cell lines with elevated ROS levels to compare cytotoxic responses and gain deeper insight into cell-type-specific efficacy. This comparative approach may help identify which subtypes are most susceptible to ROS-targeted treatment strategies and guide the design of next-generation redox-sensitive nanotherapeutics.

CONCLUSION

This study demonstrates that HNSCC cell lines differ in their basal redox states, which may influence their sensitivity to ROS-modulating therapies. These differences may offer a basis for patient stratification and personalized treatment approaches. Furthermore, the ROS-responsive NCs showed good biocompatibility and efficient cellular uptake in HNSCC models, supporting their potential as a safe drug delivery platform. While the chemotherapeutic-loaded NCs exhibited promising cytotoxic effects, their suboptimal efficacy underscores the need for further optimization to improve therapeutic outcomes and achieve effective, tumor-specific drug release.

REFERENCES

This text was supported by GenAI

1. Bray, F., Laversanne, M., Sung, H., Ferlay, J., Siegel, R. L., Soerjomataram, I. *et al.* (2024) Global cancer statistics 2022: GLOBOCAN estimates of incidence and mortality worldwide for 36 cancers in 185 countries *CA Cancer J Clin* **74**, 229-263
2. (2024) Cancer Tomorrow World Health Organization: International Agency for Research on Cancer,
3. Gormley, M., Creaney, G., Schache, A., Ingarfield, K., and Conway, D. I. (2022) Reviewing the epidemiology of head and neck cancer: definitions, trends and risk factors *Br Dent J* **233**, 780-786
4. Daniel E. Johnson, B. B., C. René Leemans, Vivian Wai Yan Lui, Julie E., and Bauman, J. R. G. (2021) Head and neck squamous cell carcinoma *Nature Reviews Disease Primers*
5. (2021) Head and Neck Cancers NIH: national cancer institute,
6. Baxi, S., Fury, M., Ganly, I., Rao, S., and Pfister, D. G. (2012) Ten years of progress in head and neck cancers *J Natl Compr Canc Netw* **10**, 806-810
7. de Martel, C., Plummer, M., Vignat, J., and Franceschi, S. (2017) Worldwide burden of cancer attributable to HPV by site, country and HPV type *Int J Cancer* **141**, 664-670
8. Blot, W. J., McLaughlin, J. K., Winn, D. M., Austin, D. F., Greenberg, R. S., Preston-Martin, S. *et al.* (1988) Smoking and drinking in relation to oral and pharyngeal cancer *Cancer Res* **48**, 3282-3287

9. Shirima, C. A., Bleotu, C., Spandidos, D. A., El-Naggar, A. K., Gradisteanu Pircalabioru, G., and Michalopoulos, I. (2024) Epithelial-derived head and neck squamous tumourigenesis (Review) *Oncol Rep* **52**,
10. Johnson, D. E., Burtness, B., Leemans, C. R., Lui, V. W. Y., Bauman, J. E., and Grandis, J. R. (2020) Head and neck squamous cell carcinoma *Nat Rev Dis Primers* **6**, 92
11. Jagadeesan, D., Sathasivam, K. V., Fuloria, N. K., Balakrishnan, V., Khor, G. H., Ravichandran, M. *et al.* (2024) Comprehensive insights into oral squamous cell carcinoma: Diagnosis, pathogenesis, and therapeutic advances *Pathol Res Pract* **261**, 155489
12. Li, H. X., Gong, Y. W., Yan, P. J., Xu, Y., Qin, G., Wen, W. P. *et al.* (2024) Revolutionizing head and neck squamous cell carcinoma treatment with nanomedicine in the era of immunotherapy *Front Immunol* **15**, 1453753
13. Ang, K. K., Harris, J., Wheeler, R., Weber, R., Rosenthal, D. I., Nguyen-Tan, P. F. *et al.* (2010) Human papillomavirus and survival of patients with oropharyngeal cancer *N Engl J Med* **363**, 24-35
14. Zhang, C., Xu, C., Gao, X., and Yao, Q. (2022) Platinum-based drugs for cancer therapy and anti-tumor strategies *Theranostics* **12**, 2115-2132
15. Weiland, A. C., Samant, S., Clain, A. E., and Martin-Harris, B. (2024) Short- and Long-Term Swallowing Outcomes in Head and Neck Cancer Patients Receiving TORS and Adjuvant Therapy *Head Neck* 10.1002/hed.28033
16. Cramer, J. D., Burtness, B., Le, Q. T., and Ferris, R. L. (2019) The changing therapeutic landscape of head and neck cancer *Nat Rev Clin Oncol* **16**, 669-683
17. Forastiere, A. A., Ismaila, N., Lewin, J. S., Nathan, C. A., Adelstein, D. J., Eisbruch, A. *et al.* (2018) Use of Larynx-Preservation Strategies in the Treatment of Laryngeal Cancer: American Society of Clinical Oncology Clinical Practice Guideline Update *J Clin Oncol* **36**, 1143-1169
18. Vlacich, G., Spratt, D. E., Diaz, R., Phillips, J. G., Crass, J., Li, C. I. *et al.* (2014) Dose to the inferior pharyngeal constrictor predicts prolonged gastrostomy tube dependence with concurrent intensity-modulated radiation therapy and chemotherapy for locally-advanced head and neck cancer *Radiother Oncol* **110**, 435-440
19. Vergeer, M. R., Doornaert, P. A., Rietveld, D. H., Leemans, C. R., Slotman, B. J., and Langendijk, J. A. (2009) Intensity-modulated radiotherapy reduces radiation-induced morbidity and improves health-related quality of life: results of a nonrandomized prospective study using a standardized follow-up program *Int J Radiat Oncol Biol Phys* **74**, 1-8
20. Lacas, B., Bourhis, J., Overgaard, J., Zhang, Q., Gregoire, V., Nankivell, M. *et al.* (2017) Role of radiotherapy fractionation in head and neck cancers (MARCH): an updated meta-analysis *Lancet Oncol* **18**, 1221-1237
21. Li, C., Fang, Y., Xu, S., Zhao, J., Dong, D., and Li, S. (2024) Nanomedicine in HNSCC therapy-a challenge to conventional therapy *Front Pharmacol* **15**, 1434994
22. Bentz, B. (2007) Head and neck squamous cell carcinoma as a model of oxidative-stress and cancer *J Surg Oncol* **96**, 190-191
23. Liang, J., Yang, B., Zhou, X., Han, Q., Zou, J., and Cheng, L. (2021) Stimuli-responsive drug delivery systems for head and neck cancer therapy *Drug Deliv* **28**, 272-284

24. An, X., Yu, W., Liu, J., Tang, D., Yang, L., and Chen, X. (2024) Oxidative cell death in cancer: mechanisms and therapeutic opportunities *Cell Death Dis* **15**, 556
25. Cairns, R. A., Harris, I. S., and Mak, T. W. (2011) Regulation of cancer cell metabolism *Nat Rev Cancer* **11**, 85-95
26. Huang, G., and Pan, S. T. (2020) ROS-Mediated Therapeutic Strategy in Chemo-/Radiotherapy of Head and Neck Cancer *Oxid Med Cell Longev* **2020**, 5047987
27. Ashcraft, K. A., Boss, M. K., Tovmasyan, A., Roy Choudhury, K., Fontanella, A. N., Young, K. H. *et al.* (2015) Novel Manganese-Porphyrin Superoxide Dismutase-Mimetic Widens the Therapeutic Margin in a Preclinical Head and Neck Cancer Model *Int J Radiat Oncol Biol Phys* **93**, 892-900
28. Toledo, M. M., De Souza Goncalves, B., Colodette, N. M., Chaves, A. L. F., Muniz, L. V., De, A. R. R. I. M. *et al.* (2021) Tumor Tissue Oxidative Stress Changes and Na, K-ATPase Evaluation in Head and Neck Squamous Cell Carcinoma *J Membr Biol* **254**, 475-486
29. Pedro, N. F., Biselli, J. M., Maniglia, J. V., Santi-Neto, D., Pavarino, E. C., Goloni-Bertollo, E. M. *et al.* (2018) Candidate Biomarkers for Oral Squamous Cell Carcinoma: Differential Expression of Oxidative Stress-Related Genes *Asian Pac J Cancer Prev* **19**, 1343-1349
30. Ionescu, C., Kamal, F. Z., Ciobica, A., Halitchi, G., Burlui, V., and Petroaie, A. D. (2024) Oxidative Stress in the Pathogenesis of Oral Cancer *Biomedicines* **12**,
31. Cruz-Gregorio, A., Martinez-Ramirez, I., Pedraza-Chaverri, J., and Lizano, M. (2019) Reprogramming of Energy Metabolism in Response to Radiotherapy in Head and Neck Squamous Cell Carcinoma *Cancers (Basel)* **11**,
32. Li, D., Kou, Y., Gao, Y., Liu, S., Yang, P., Hasegawa, T. *et al.* (2021) Oxaliplatin induces the PARP1-mediated parthanatos in oral squamous cell carcinoma by increasing production of ROS *Aging (Albany NY)* **13**, 4242-4257
33. Zhang, W., Chen, S., Bai, Z., Gan, M., Chen, M., Zhang, Y. *et al.* (2024) Photodynamic Therapy for Oral Squamous Cell Carcinoma: Current Status, Challenges, and Prospects *Int J Nanomedicine* **19**, 10699-10710
34. Ji, W. O., Lee, M. H., Kim, G. H., and Kim, E. H. (2019) Quantitation of the ROS production in plasma and radiation treatments of biotargets *Sci Rep* **9**, 19837
35. Yarangsee, P., Khacha-Ananda, S., Pitchakarn, P., Intayoung, U., Sriuan, S., Karinchai, J. *et al.* (2024) A Nonclinical Safety Evaluation of Cold Atmospheric Plasma for Medical Applications: The Role of Genotoxicity and Mutagenicity Studies *Life (Basel)* **14**,
36. Li, X., Rui, X., Li, D., Wang, Y., and Tan, F. (2022) Plasma oncology: Adjuvant therapy for head and neck cancer using cold atmospheric plasma *Front Oncol* **12**, 994172
37. Stevens, L. M. L.-M. E. N. J. B. C. W. C. C. C. H. H. K. A. K. J. P. M. (2022) What Do We Mean When We Say Nanomedicine? *ACS Nano*
38. Han, Y., Wen, P., Li, J., and Kataoka, K. (2022) Targeted nanomedicine in cisplatin-based cancer therapeutics *J Control Release* **345**, 709-720
39. Sun, T., and Jiang, C. (2023) Stimuli-responsive drug delivery systems triggered by intracellular or subcellular microenvironments *Adv Drug Deliv Rev* **196**, 114773

40. Majumder, J., and Minko, T. (2021) Multifunctional and stimuli-responsive nanocarriers for targeted therapeutic delivery *Expert Opin Drug Deliv* **18**, 205-227
41. Wang, F., Wang, M., Zhao, L., Li, Q. (2019) A new biosafe reactive oxygen species responsive nanoplatform for targeted oral squamous cell carcinoma therapy *Materials express* **9**,
42. Zhou, J., Li, K., Zang, X., Xie, Y., Song, J., and Chen, X. (2023) ROS-responsive Galactosylated-nanoparticles with Doxorubicin Entrapment for Triple Negative Breast Cancer Therapy *Int J Nanomedicine* **18**, 1381-1397
43. Zhang, L., Zhang, S., Li, M., Li, Y., Xiong, H., Jiang, D. *et al.* (2021) Reactive oxygen species and glutathione dual responsive nanoparticles for enhanced prostate cancer therapy *Mater Sci Eng C Mater Biol Appl* **123**, 111956
44. Chen, Y., Cai, S., Liu, F. Y., and Liu, M. (2025) Advancing oral cancer care: nanomaterial-driven diagnostic and therapeutic innovations *Cell Biol Toxicol* **41**, 90
45. Canning, M., Guo, G., Yu, M., Myint, C., Groves, M. W., Byrd, J. K. *et al.* (2019) Heterogeneity of the Head and Neck Squamous Cell Carcinoma Immune Landscape and Its Impact on Immunotherapy *Front Cell Dev Biol* **7**, 52
46. Tiscornia, G., Singer, O., and Verma, I. M. (2006) Production and purification of lentiviral vectors *Nat Protoc* **1**, 241-245
47. Zhang, C., Qin, Y., Deng, C., Zhu, N., Shi, Y., Wang, W. *et al.* (2023) GSH-specific fluorescent probe for sensing, bioimaging, rapid screening of natural inhibitor Celastrol and ccRCC theranostics *Anal Chim Acta* **1248**, 340933
48. Nayak, S., Caz, N., Derveaux, E., Smeets, S., Cardeynaels, T., Wolfs, E. *et al.* (2025) Reactive oxygen species responsive dextran-thioketal conjugate nanocarriers for the delivery of hydrophilic payloads *Carbohydr Polym* **356**, 123375
49. Castaldo, S. A., Freitas, J. R., Conchinha, N. V., and Madureira, P. A. (2016) The Tumorigenic Roles of the Cellular REDOX Regulatory Systems *Oxid Med Cell Longev* **2016**, 8413032
50. Nguyen, T., Nioi, P., and Pickett, C. B. (2009) The Nrf2-antioxidant response element signaling pathway and its activation by oxidative stress *J Biol Chem* **284**, 13291-13295
51. Huh, H. D., Sub, Y., Oh, J., Kim, Y. E., Lee, J. Y., Kim, H. R. *et al.* (2023) Correction: Reprogramming anchorage dependency by adherent-to-suspension transition promotes metastatic dissemination *Mol Cancer* **22**, 135
52. Li, A. E., Ito, H., Rovira, II, Kim, K. S., Takeda, K., Yu, Z. Y. *et al.* (1999) A role for reactive oxygen species in endothelial cell anoikis *Circ Res* **85**, 304-310
53. Binek, A., Rojo, D., Godzien, J., Ruperez, F. J., Nunez, V., Jorge, I. *et al.* (2019) Flow Cytometry Has a Significant Impact on the Cellular Metabolome *J Proteome Res* **18**, 169-181
54. Patterson, J. C., Joughin, B. A., van de Kooij, B., Lim, D. C., Lauffenburger, D. A., and Yaffe, M. B. (2019) ROS and Oxidative Stress Are Elevated in Mitosis during Asynchronous Cell Cycle Progression and Are Exacerbated by Mitotic Arrest *Cell Syst* **8**, 163-167 e162
55. Kuo, C. L., Ponneri Babuharisankar, A., Lin, Y. C., Lien, H. W., Lo, Y. K., Chou, H. Y. *et al.* (2022) Mitochondrial oxidative stress in the tumor microenvironment and cancer

immunoescape: foe or friend? *J Biomed Sci* **29**, 74
56. Kim, Y., and Lee, H. M. (2024) Acidic solvent improves cisplatin action in in-vitro *Biochem Biophys Res Commun* **712-713**, 149936
57. Zhang, H., Huang, S., Yang, X., and Zhai, G. (2014) Current research on hyaluronic acid-drug bioconjugates *Eur J Med Chem* **86**, 310-317
58. Shingel, K., Selyanin, M., et al. (2017) Solid dispersions of drugs in hyaluronan matrix: The role of the biopolymer in modulating drug activity *in vivo Journal of Drug Delivery Science and Technology*
59. Cai, S., Xie, Y., Bagby, T. R., Cohen, M. S., and Forrest, M. L. (2008) Intralymphatic chemotherapy using a hyaluronan-cisplatin conjugate *J Surg Res* **147**, 247-252
60. Khan, M. S., Gowda, B. H. J., Nasir, N., Wahab, S., Pichika, M. R., Sahebkar, A. *et al.* (2023) Advancements in dextran-based nanocarriers for treatment and imaging of breast cancer *Int J Pharm* **643**, 123276
61. Rinaldi, A., Caraffi, R., Grazioli, M. V., Oddone, N., Giardino, L., Tosi, G. *et al.* (2022) Applications of the ROS-Responsive Thioketal Linker for the Production of Smart Nanomedicines *Polymers (Basel)* **14**,
62. Tu, Y., Zhang, W., Fan, G., Zou, C., Zhang, J., Wu, N. *et al.* (2023) Paclitaxel-loaded ROS-responsive nanoparticles for head and neck cancer therapy *Drug Deliv* **30**, 2189106
63. Kim, J., Kim, S., Et al. (2019) ROS-responsive thioether-based nanocarriers for efficient pro-oxidant cancer therapy *Journal of Industrial and Engineering Chemistry*

Acknowledgements – LvH is grateful for EW and NC to be able to complete this research at the Laboratory for Functional Imaging and Research on Stem Cells (FIERCE Lab), UHasselt.
Author contributions – LvH, NC and ES performed experiments. LvH and NC performed data analysis. MP provided the ROS-responsive nanocarriers.